Remote Sensing of Environment 231 (2019) 111275

Contents lists available at ScienceDirect

Remote Sensing of Environment

journal homepage: www.elsevier.com/locate/rse

Accounting for permafrost creep in high-resolution snow depth mapping by modelling sub-snow ground deformation

Jason Goetz[a,*], Paul Fieguth[b], Keyvan Kasiri[b,c], Xavier Bodin[d], Marco Marcer[d,e], Alexander Brenning[a]

[a] Department of Geography, Friedrich Schiller University Jena, Germany
[b] Department of Systems Design Engineering, University of Waterloo, Canada
[c] Borealis AI, Toronto, Canada
[d] Laboratoire EDYTEM, CNRS, Université Savoie Mont-Blanc, France
[e] Laboratoire PACTE, CNRS, Science Po Grenoble, Université Grenoble Alpes, France

ARTICLE INFO

Edited by Menghua Wang

Keywords:
Snow depth
Rock glacier
Permafrost creep
Non-rigid registration
Free-form deformation
Surface displacement
Digital elevation models
LiDAR
Structure-from-motion photogrammetry

ABSTRACT

Snow depth estimation derived from high-resolution digital elevation models (DEMs) can lead to improved understanding of the spatially highly heterogeneous nature of snow distribution, as well as help us improve our knowledge of how snow patterns influence local geomorphic processes. Slope deformation processes such as permafrost creep can make it challenging to acquire a snow-free DEM that matches the sub-snow topography at the time of the associated snow-covered DEM, which can cause errors in the computed snow depths. In this study, we illustrate how modelling changes in the sub-snow topography can reduce errors in snow depths derived from DEM differencing in an area of permafrost creep. To model the sub-snow topography, a surface deformation model was constructed by performing non-rigid registration based on B-splines of two snow-free DEMs. Seasonal variations in creep were accounted for by using an optimization approach to find a suitable value to scale the deformation model based on in-situ snow depth measurements or the presence of snow-free areas corresponding to the date of the snow-covered DEM. This scaled deformation model was used to transform one of the snow-free DEMs to estimate the sub-snow topography corresponding to the date of the snow-covered DEM. The performance of this method was tested on an active rock glacier in the southern French Alps for two surveys dates, which were conducted in the winter and spring of 2017.

By accounting for surface displacements caused by permafrost creep, we found that our method was able to reduce the errors in the estimated snow depths by up to 33% (an interquartile range reduction of 11 cm) compared to using the untransformed snow-free DEM. The accuracy of the snow depths only slightly improved (root-mean-square error decrease of up to 3 cm). Greater reductions in error were observed for the snow depths calculated for the date that was furthest (i.e., the winter survey) in time from the snow-free DEM. Additionally, we found that our approach to scaling the deformation model has promising potential to be adapted for monitoring seasonal variations in permafrost creep by combining in-situ snow depth measurements with high-resolution surface deformation models.

1. Introduction

A combination of complex terrain with variable snow accumulation and ablation processes can result in a spatially highly heterogeneous snow distribution (Elder et al., 1991; Blöschl, 1999; Deems et al., 2006; Erickson et al., 2005; Winstral et al., 2013; Grünewald et al., 2013). In mountain areas, snow cover can be an important control of surface deformation rates related to geomorphic processes such as permafrost creep (Ikeda et al., 2008) and shallow-landslides (Matsuura et al., 2003; Okamoto et al., 2018). Snow cover also plays an important role in ground temperatures (Hasler et al., 2011; Luetschg and Haeberli, 2007; Haberkorn et al., 2016). Therefore, providing detailed and accurate mapping of the heterogeneous snow patterns would allow a continued improvement in our understanding of snow distribution and how to model it (Sturm, 2015; Bhardwaj et al., 2016) to better describe the impact of snow cover on mountain geomorphic processes (Swift et al., 2014).

Currently, the best method to capture the spatial variations in snow

* Corresponding author.
E-mail address: jason.goetz@uni-jena.de (J. Goetz).

https://doi.org/10.1016/j.rse.2019.111275
Received 29 October 2018; Received in revised form 6 June 2019; Accepted 19 June 2019
Available online 27 June 2019

depth is the use of high-resolution digital elevation models (DEMs). High-resolution mapping of snow depth can be achieved using any or a combination of available techniques for deriving high-resolution elevation models of the Earth's surface. Some common techniques already applied include laser altimetry (LiDAR; Deems et al., 2006; Prokop et al., 2008; Helfricht et al., 2012; Draebing et al., 2017), digital photogrammetry (Bühler et al., 2015; Marti et al., 2016; Grünewald et al., 2014; Bühler et al., 2012), and structure-from-motion multi-view stereo (SFM-MVS) 3D reconstruction (Nolan et al., 2015; Vander Jagt et al., 2015; Bühler et al., 2016; Michele et al., 2016; Harder et al., 2016).

Snow depth based on high-resolution elevation data can be computed by differencing co-registered elevation models obtained for snow-covered and snow-free conditions. The differencing can be applied to surface elevations represented as 3D point clouds or a corresponding DEM (Deems et al., 2013). It is typically assumed that the surface topography beneath the snow-cover remains unchanged during the period between the acquisition of the snow-covered and snow-free conditions. However, any change in the surface topography between the acquisition dates can contribute to errors in the computed snow depth measurements (Nolan et al., 2015; Bernard et al., 2017; Avanzi et al., 2018). For this reason, applying this approach in mountain areas can be challenging due to on-going changes in surface topography caused by permafrost creep (Haeberli et al., 2006; Kääb et al., 2003), and other slope deformation processes (Arenson et al., 2016). Therefore, such changes in surface topography should be accounted for in the snow-free elevation model to reduce errors in the computed high-resolution snow depths, as well as to provide more reliable snow distribution data for analysis on the impacts of snow on local variations in geomorphic processes. In this paper, we propose that a kinematic model of surface displacements can be used to account for changes in topography due to permafrost creep.

The spatial pattern of creeping mountain permafrost is often monitored using surface displacement fields obtain from processing remote sensing data (Arenson et al., 2016). Most commonly, surface displacements fields are determined from multi-temporal optical imagery using image matching techniques (Scambos et al., 1992; Kääb, 2002; Heid and Kääb, 2012; Kääb, 2005; Debella-Gilo and Kääb, 2011; Kraaijenbrink et al., 2016; Evans, 2000). Image matching has also been applied to high-resolution DEMs to produce detailed surface displacement maps of glacial ice (Abdalati and Krabill, 1999), slow-moving landslides (Ghuffar et al., 2013) and permafrost creep (Dall'Asta et al., 2017; Bodin et al., 2018). The use of DEMs for image matching has the advantage of avoiding the requirement of having the paired survey data acquired under similar lighting conditions (Kääb, 2005), and have been found to obtain a greater number of matched pixels than high-resolution optical imagery (Dall'Asta et al., 2017).

Due to its simplicity, normalized cross-correlation is one of the most commonly applied methods for image matching using remote sensing data (Kääb, 2005; Heid and Kääb, 2012). However, this method typically requires post-processing to remove erroneous matches (Heid and Kääb, 2012; Kääb, 2005; Debella-Gilo and Kääb, 2012). Also, large data gaps in surface displacement maps can occur in areas where the image matching algorithm had difficulties detecting corresponding surface features (Bodin et al., 2018; Kääb, 2005). To overcome these issues, image registration techniques, in particular deformable or non-rigid registration, may be a good alternative to using image matching techniques alone for mapping surface displacement field since they are designed to provide a spatially continuous field of displacements for monitoring deformation of objects over time (Hill et al., 2001).

Image registration is the process of aligning images by finding a spatial transformation that maps the pixels from one image to corresponding pixels in another image (Hill et al., 2001). Like image matching techniques, the aligning of two images for registration can be feature- and/or intensity-based, where features refer to corresponding points identified in the images either manually or automatically. The alignment based on features aims to minimize the distance between points, where intensity-based alignment involves minimizing a cost function that measures the similarity between a set of corresponding pixels between images (Yoo, 2004).

Non-rigid image registration allows for a non-uniform mapping of corresponding pixels between images (Rueckert et al., 1999; Crum et al., 2004). The resulting transformation is a deformation field that tracks the displacement of every pixel from one image to another. To ensure that physically meaningful deformations are recorded by the transformation, regularization terms can be applied (Crum et al., 2004; Rueckert et al., 1999). Given this ability to record realistic changes in morphology, non-rigid image registration techniques have promising potential for producing a model of creep-related surface deformations for an entire scene. Additionally, to our knowledge, non-rigid image registration techniques have yet to be applied for monitoring surface displacements of Earth surface landforms.

In this study, we present a method to reduce errors in snow depths computed from high-resolution DEMs in an area of permafrost creep based on surface deformation modelling. The changes in the sub-snow topography caused by permafrost creep movement during snow-cover conditions are estimated by transforming a snow-free DEM using a kinematic model of surface deformations. This model is obtained by performing non-rigid registration using a free-form deformation model based on B-splines of two snow free DEMs. To account for variations in creep rates over time, the resulting displacement field is scaled and then used to transform one of the snow-free DEMs to estimate the sub-snow surface topography at the time of the snow-covered DEM. The performance of our method is evaluated using in-situ bare-ground topography and snow depth measurements.

2. Methods

2.1. Study site and data

Our study site is the Laurichard rock glacier in the Combe de Laurichard catchment, Écrins National Park, located in the southern French Alps (45.01°N, 6.37°E). It is an active, tongue-shaped rock glacier extending from 2650 m a.s.l. (the headwall) to 2450 m a.s.l. (the front) with a width varying from about 100 m to 200 m. Based on expert knowledge of the study site (Bodin et al., 2009; Bodin et al., 2018), areas on the rock glacier were considered as active terrain, and the remaining terrain was considered as stable. The delineation of active and stable terrain was based on a map of the rock glacier (Fig. 1). The movement rate of the rock glacier, measured as the mean annual surface velocity (0.39 to 1.44 m/yr; Bodin et al., 2009), is typical of deep-seated permafrost creep (Haeberli et al., 2006). Similarly to many rock glaciers in the Alps (e.g., Delaloye et al., 2008; Kellerer-Pirklbauer et al., 2018), the Laurichard rock glacier experiences interannual fluctuation of its velocity (Thibert et al., 2018). The spatial pattern of displacements has been generally consistent over the past 10 years (Bodin et al., 2018). Consistent spatial patterns of rock glacier movement have also been observed by others (Ikeda et al., 2008).

Our method for accounting for permafrost creep in snow depth mapping was applied to two dates, February 22, 2017 and June 2, 2017, which represent the snow cover conditions during the winter accumulation and spring melt periods. A snow-free DEM was obtained on October 5, 2017. The DEMs were acquired by performing SFM-MVS 3D reconstruction with Agisoft's PhotoScan (version 1.41) to images collected from unmanned aerial vehicle (UAV) surveys using a DJI Phantom 4 quadcopter. The UAV surveys and PhotoScan processing used the same methods as Goetz et al. (2018). The winter DEM (referred to as Feb-2017 DEM) was mainly snow covered except for some large rock debris and boulders located on the rock glacier (Fig. 1). The spring DEM (Jun-2017 DEM) was partially (75%) snow covered.

An available DEM acquired on August 16–17, 2012 (Aug-2012 DEM) and the Oct-2017 DEM were used to find a non-rigid image transformation that captures the permafrost creep related surface

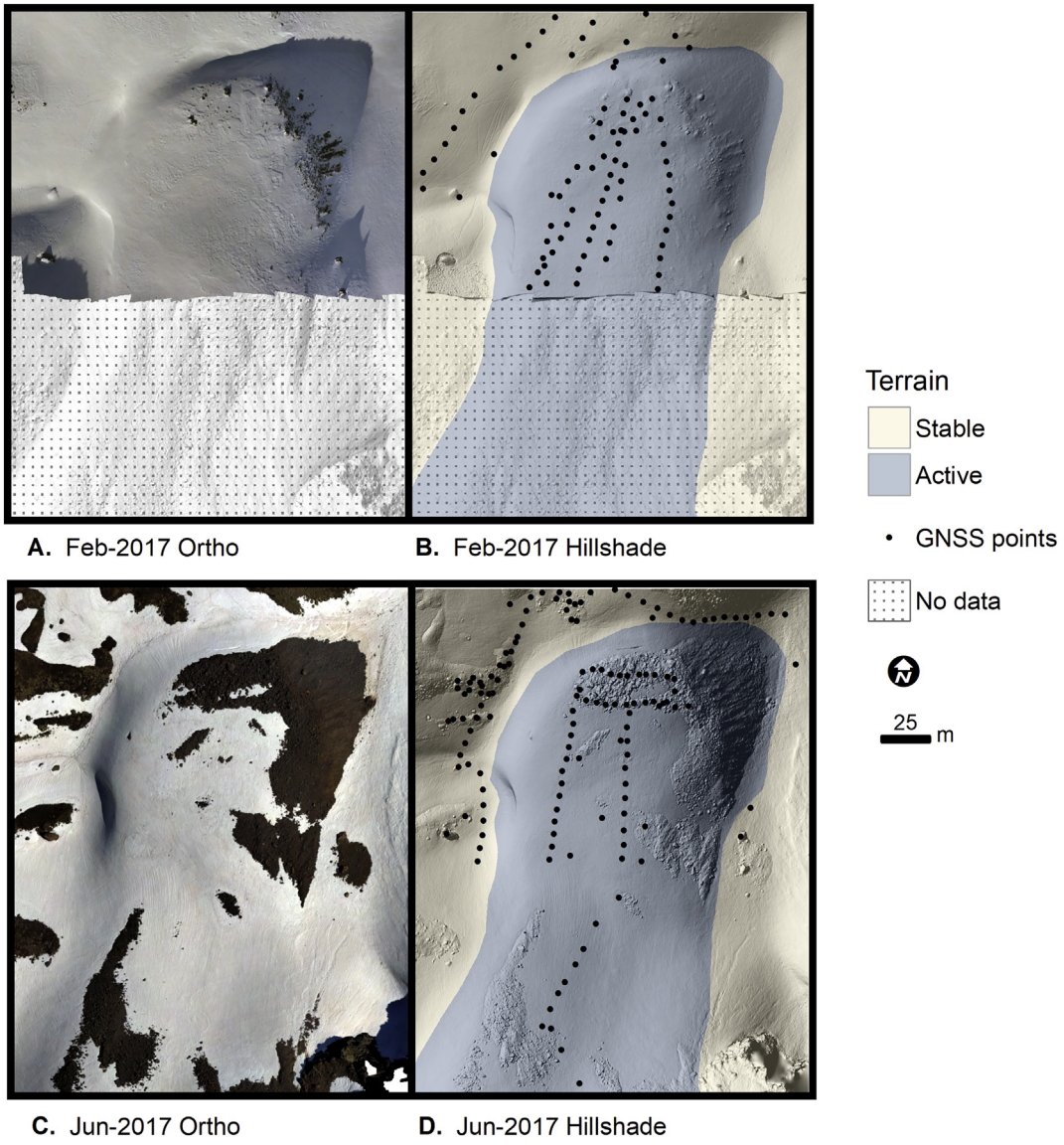

Fig. 1. Orthomosaics of the snow-covered scenes on 22-Feb-2017 (A.) and 2-Jun-2017 (C). Distribution of field surveyed GNSS points of snow-free areas and snow-probed measured. An outline of the stable and active terrain areas overlays the hillshade models of the Feb-2017 and Jun-2017 DEMs. The winter Feb-2017 DEM covers about half the area of the spring Jun-2017 DEM.

deformation patterns. The Aug 2012 DEM was derived from airborne-laser scanning (ALS; Cessna 206 with a Riegl LMS Q680i laser scanner) (Bodin et al., 2018). All of the DEMs used in our study were sampled (bilinear interpolation) to have a 10 cm × 10 cm spatial resolution.

The vertical accuracies of the DEMs were assessed from Global Navigation Satellite System (GNSS) surveyed elevation measurements (positional accuracy ≤2 cm at 1σ). The resulting RMSE for the Jun-2017, Oct-2017 and Aug-2012 DEMs were 7.8 cm, 9.1 cm and 2 cm, respectively (Table 1). The RMSE for the Aug-2012 DEM was based on a set of GNSS surveyed points of artificial flat surfaces measured during the acquisition of the airborne LiDAR data (Bodin et al., 2018).

2.2. Mapping snow depth from DEMs

Estimating snow depth $\widehat{D}(\boldsymbol{x})$ for a continuous surface at locations $\boldsymbol{x}$ for a given time t_0 can be calculated as

$$\widehat{D}_{t_0}(\boldsymbol{x}) = S_{t_0}(\boldsymbol{x}) - \widehat{Z}_{t_0}(\boldsymbol{x}), \quad (1)$$

Table 1
Summary of data sets used for estimating snow depth. The vertical accuracy is based on a set of GNSS observations (N) surveyed for each date.

	Data overview			
Label	Feb-2017 DEM	Jun-2017 DEM	Oct-2017 DEM	Aug-2012 DEM
Acquisition data	22 Feb 2017	2 Jun 2017	5 Oct 2017	16/17 Aug 2012
Description	Snow covered	Snow covered	Snow free	Snow free
Method	UAV SFM-MVS	UAV SFM-MVS	UAV SFM-MVS	Airborne LiDAR
Vertical accuracy (RMSE)	4.8 cm (N = 85)	7.6 cm (N = 118)	9.1 cm (N = 130)	2 cm (N = 45)
No. of snow probe observations	N_D = 63	N_D = 58	–	–

where $S_{t_0}(\boldsymbol{x})$ and $\widehat{Z}_{t0}(\boldsymbol{x})$ are DEMs consisting of elevations for the snow-covered surface and the estimated sub-snow topography, respectively. Since the actual sub-snow topography $Z_{t_0}(\boldsymbol{x})$ at the time of the acquired snow-covered DEM is an unknown, the acquired snow-free DEM $Z_{t_1}(\boldsymbol{x})$ can be used to estimate $\widehat{Z}_{t0}(\boldsymbol{x})$ the sub-snow topography. Given an area with little to no change in the ground topography over time, the estimated sub-snow topography is usually assumed to equal the elevations at the time of a snow-free elevation model either obtained before or after the time of the snow-covered DEM. However, in the case that the surface topography of the snow-free elevation model is likely different than the actual sub-snow topography, meaning there are active deformation processes occurring, the sub-snow topography can be obtained by transforming a snow-free DEM $Z_{t_1}(\boldsymbol{x})$ to represent the bare-ground topography conditions at the time of the snow-covered DEM.

To determine this transformation $\boldsymbol{T_u}(\boldsymbol{x})$, we treat this as a registration problem which aims to find the displacement field $\boldsymbol{u}(\boldsymbol{x})$ that makes the snow-free DEM $Z_{t_1}(\boldsymbol{x} + \boldsymbol{u}(\boldsymbol{x}))$ as close as possible to the actual sub-snow topography $Z_{t_0}(\boldsymbol{x})$. Since the sub-snow topography is unknown, we estimate the transformation by scaling displacements $\boldsymbol{a}(\boldsymbol{x})$, which have been determined a priori, that map the general surface deformation patterns of the bare-ground topography. We define the estimate of the transformation $\widehat{\boldsymbol{T}}_u(\boldsymbol{x})$ as

$$\widehat{\boldsymbol{T}}_u(\boldsymbol{x}, \hat{c}) = \boldsymbol{x} + \hat{c}\boldsymbol{a}(\boldsymbol{x}); \tag{2}$$

the estimated sub-snow topography is therefore determined by applying the estimated transformation to the snow-free DEM $Z_{t_1}(\boldsymbol{x})$

$$\widehat{Z}_{t_0}(\boldsymbol{x}) = Z_{t1}(\widehat{\boldsymbol{T}}_u(\boldsymbol{x}, \hat{c})), \tag{3}$$

where $\hat{c}$ is an estimate of a scale factor c, used to find displacements $\boldsymbol{u}(\boldsymbol{x})$ by scaling the known displacements $\boldsymbol{a}(\boldsymbol{x})$. The scale factor c is basically a measure of the position of the deforming topography relative to the reference snow-free topography $Z_{t_1}(\boldsymbol{x})$.

The general deformation pattern $\boldsymbol{a}(\boldsymbol{x})$ can be obtained by finding a transformation $\boldsymbol{T_a}(\boldsymbol{x})$ from non-rigid registration that makes the snow-free DEM $Z_{t_1}(\boldsymbol{T_a}(\boldsymbol{x}))$ as close as possible to another snow-free DEM, $Z_{t_2}(\boldsymbol{x})$, where the transformation $\boldsymbol{T_a}(\boldsymbol{x}) = \boldsymbol{x} + \boldsymbol{a}(\boldsymbol{x})$ is a model of the surface deformation. Note that the change in time between the snow-free DEMs, $Z_{t_1}(\boldsymbol{x})$ and $Z_{t_2}(\boldsymbol{x})$, should be large enough to detect surface deformations. The snow-free DEM $Z_{t_1}(\boldsymbol{x})$ should be defined as the snow-free elevation model that is closest in time to the snow-covered DEM since the interpolation of an estimated sub-snow DEM will likely become more unstable as the time between the acquisition dates of the snow-covered and snow-free DEMs increases. Additionally, the accuracy of the estimated transformation $\widehat{\boldsymbol{T}}_u(\boldsymbol{x})$ of the snow-free DEM highly depends on how well the model of surface displacements, as determined by $\boldsymbol{T_a}(\boldsymbol{x})$, represents the general deformation of the bare-ground surface topography over time, and on our ability to determine a suitable scale factor c.

A displacement field mapped using deformable (non-rigid) image registration will have a vector magnitude and direction for each corresponding DEM grid cell that can vary spatially. It is therefore assumed that the displacements $\boldsymbol{a}(\boldsymbol{x})$, which are used to model the creeping processes acting on the landscape, have a spatial pattern that remains similar during the period between snow-free DEMs, $Z_{t_1}(\boldsymbol{x})$ and $Z_{t_2}(\boldsymbol{x})$. A constant displacement rate is not assumed. Instead, by finding an optimal scale value for a given date, we allow our model to account for variations in displacement rates over time.

2.2.1. Finding an optimal scale factor

Given that the transformation $\boldsymbol{T_a}(\boldsymbol{x})$ provides a good model of the surface deformation movements, the ability to produce a good estimation of the sub-snow topography for a given time depends on the scaling of this transformation. In this study we apply several methods for estimating an optimal scale factor $\hat{c}$ based on manually mapped surface displacements, snow-free areas in the snow-covered DEM and in-situ snow depth measurements.

Provided there are exposed blocks that can have their movement tracked from the snow-free DEM $Z_{t_1}(\boldsymbol{x})$ to the snow-covered DEM $S_{t_0}(\boldsymbol{x})$, we may determine $\hat{c}$ as the average ratio of the magnitude of displacements observed from matching displaced features in $Z_{t_1}(\boldsymbol{x})$ to $S_{t_0}(\boldsymbol{x}_i)$ for a set corresponding snow-free (i.e., bare-ground) cell locations, Ω_Z, within the domain of the snow-covered DEM $S_{t_0}(\boldsymbol{x})$,

$$\hat{c} := \frac{1}{|\Omega_Z|} \sum_{x_i \in \Omega_Z} \frac{\boldsymbol{v}(\boldsymbol{x}_i)}{\boldsymbol{a}(\boldsymbol{x}_i)} \tag{4}$$

where $\boldsymbol{v}(\boldsymbol{x}_i)$ are displacements mapped from locations in the snow-free DEM $Z_{t_1}(\boldsymbol{x}_i)$ to the corresponding snow-free cell locations in the snow-covered DEM $S_{t_0}(\boldsymbol{x}_i)$, $\boldsymbol{a}(\boldsymbol{x}_i)$ are the displacements from transformation $\boldsymbol{T_a}(\boldsymbol{x})$, and $|\Omega_Z|$ is the number of snow-free cell locations. The matched features in $Z_{t_1}(\boldsymbol{x}_i)$ and $S_{t_0}(\boldsymbol{x}_i)$ can be mapped manually, or, depending on the magnitude of the mapped displacements $\boldsymbol{v}(\boldsymbol{x}_i)$, an automatic feature extraction algorithm such as the scale-invariant feature transform (SIFT; Lowe, 2004) may be applied.

Alternatively, the estimated scale factor $\hat{c}$ can be optimized using snow-free cells in locations of active terrain in the snow-covered DEM $S_{t_0}(\boldsymbol{x}_i)$ (e.g., during snow melt conditions) to iteratively calculate the estimated sub-snow topography $\widehat{Z}_{t_0}(\boldsymbol{x}_i)$ with different scale factor c values. The optimal estimated $\hat{c}$ value would result in the an estimated sub-snow topography $\widehat{Z}_{t_0}(\boldsymbol{x}_i)$ that has the greatest similarity to the snow-free cells in the snow-covered DEM $S_{t_0}(\boldsymbol{x}_i)$, such as defined by the root mean squared error (RMSE),

$$\hat{c} := \underset{c}{\operatorname{argmin}} \operatorname{RMSE}_Z(S_{t_0}(\boldsymbol{x}), \widehat{Z}_{t_0}(\boldsymbol{x}, c)) \tag{5}$$

where

$$\operatorname{RMSE}_Z(S_{t_0}(\boldsymbol{x}), \widehat{Z}_{t_0}(\boldsymbol{x}, c)) = \sqrt{\frac{1}{|\Omega_Z|} \sum_{x_i \in \Omega_Z} (S_{t_0}(\boldsymbol{x}_i) - \widehat{Z}_{t_0}(\boldsymbol{x}_i, c))^2} \tag{6}$$

In the scenario where there are no snow-free areas, a set of snow-probe recorded depths in the active terrain, Ω_D within the domain of $S_{t_0}(\boldsymbol{x})$, can take the place of snow-free areas to iteratively search for an optimal scale factor. The locations of the snow-depths should be highly accurate to match the location accuracy of the DEMs: e.g., the snow-depth locations determined from a Global Navigation Satellite System (GNSS) survey. Here, the RMSE is determined for the number of observed snow depth locations $|\Omega_D|$

$$\hat{c} := \underset{c}{\operatorname{argmin}} \operatorname{RMSE}_D(S_{t_0}(\boldsymbol{x}), \widehat{Z}_{t_0}(\boldsymbol{x}, c)) \tag{7}$$

where

$$\operatorname{RMSE}_D(D(\boldsymbol{x}), \widehat{D}(\boldsymbol{x}, c)) = \sqrt{\frac{1}{|\Omega_D|} \sum_{x_i \in \Omega_D} (D(\boldsymbol{x}_i) - \widehat{D}(\boldsymbol{x}_i, c))^2} \tag{8}$$

2.3. Modelling surface deformation

Rock glacier surface displacements from the snow free DEMs, $Z_{t_1}(\boldsymbol{x})$ and $Z_{t_2}(\boldsymbol{x})$, were obtained by performing non-rigid registration using a free-form deformation model based on B-splines (Rueckert et al., 1999). In general, B-splines can be used to create a smooth, continuous and deformable image transformation by manipulating a mesh of control points embedded in an image. A larger spacing of the mesh control points results in modelling more global deformations, while smaller spacing captures local deformations (Rueckert et al., 1999). Thus, a hierarchical multi-resolution approach that uses large to small mesh spacing can model deformations occurring at different scales.

For this paper, we used the bUnwarpJ algorithm for multi-resolution, elastic and consistent 2D image registration represented by B-Splines. bUnwarpJ, which was developed by Arganda-Carreras et al. (2006) is available as a plugin in ImageJ, an open-source image processing software (Schindelin et al., 2015). Its registration process can be

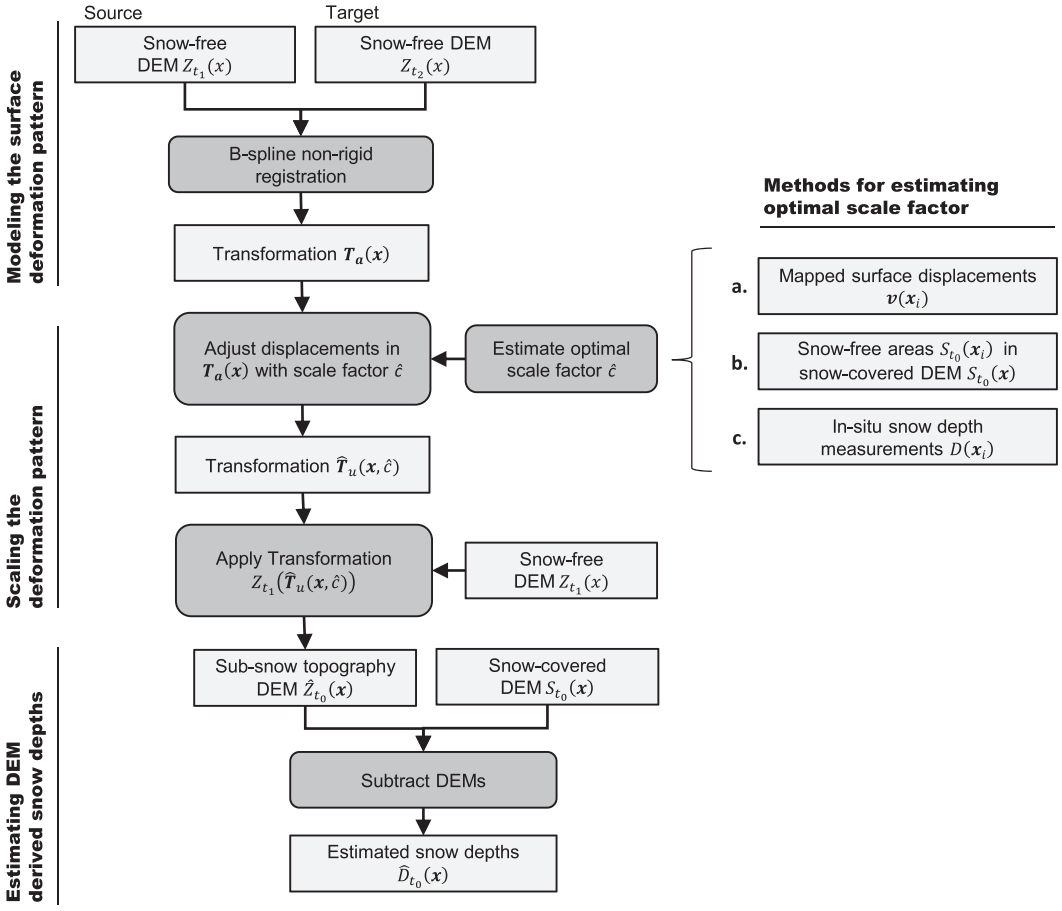

Fig. 2. A flowchart outlining the processes involved in estimating the sub-snow topography using non-rigid registration. The source and target snow-free DEMs used to model the general surface deformation pattern related to permafrost creep were the Oct-2017 and Aug-2012 DEMs, respectively. The optimal scale factor $\hat{c}$ was obtained from mapped surface displacements, snow-free areas or in-situ snow-depth measurements. $\hat{c}$ was optimized for the corresponding snow-cover date: either February 22, 2017 or June 2, 2017.

guided using image intensity, a consistency constraint, vector regularization and/or a set of landmarks. This algorithm has already been applied for various biological image analysis problems (Komsta et al., 2011; Grocott et al., 2016; Ku et al., 2016).

The bUnwarpJ algorithm is designed to perform bidirectional registration (forward and reverse directions), $Z_{t_2} \rightarrow Z_{t_1}$ and $Z_{t_2} \leftarrow Z_{t_1}$. Bidirectional registration can help reduce the number of ambiguous correspondences between the forward and reverse transformation, which may result in improving the registration accuracy (Johnson and Christensen, 2002). The Oct-2017 DEM was used as the source image (Z_{t_1}), and the Aug-2012 DEM as the target image (Z_{t_2}). The bUnwarpJ settings for the multi-resolution iterations were set to initiate with a "Fine" deformation and finish with "Super fine" deformation. In our case, the initial deformation could be set to "Fine" since the DEMs were already georectified, and as we are interested in the local deformations between the DEMs. We also set the registration to use both image intensity and feature points; these weights were set to 1. The consistency weight was left at the default value of 10. At first, we experimented with the use of automatic feature detection for extracting corresponding points; however, it was evident that some of the rock debris displacements occurring between 2012 and 2017 were too large to find accurate matches. As a result, we manually identified 233 corresponding points across the scene to assist in the image registration process. DEM-derived hillshade models were used to help identify the corresponding points.

The resulting direct (or forward) B-spline transformation, $Z_{t_2} \rightarrow Z_{t_1}$, was used to model the general deformation patterns as a transformation function $\boldsymbol{T_a}(\boldsymbol{x})$. This transformation was converted from the B-spline parameters to a transformation format containing the x and y direction displacements for each grid cell (i.e., the displacement field $\boldsymbol{a}(\boldsymbol{x})$). Since bUnwarpJ is a 2D image registration method, it only describes the horizontal (x,y) movement of the corresponding points overtime. To determine the 3D displacement (x,y,z) required to interpolate the elevations to estimate the sub-snow topography, we used the change in elevation of the corresponding points between snow-free DEMs, Z_{t_1} and Z_{t_2}, to find the displacement in the z direction. The resulting (x,y,z) displacements representing $\boldsymbol{a}(\boldsymbol{x})$ were scaled using an estimated scale factor $\hat{c}$ and applied to transform the snow-free DEM Z_{t_1} to estimate the sub-snow topography (Eq. (2)). After the transformation $\hat{\boldsymbol{T}}_{\boldsymbol{u}}(\boldsymbol{x},\hat{c})$ is applied, there may be some grid cells in the estimated DEM $\hat{Z}_{t_0}(\boldsymbol{x})$ without an assigned value for which interpolation is needed. Inverse distance weighting (IDW; Shepard, 1968) was used to fill these missing elevation values.

2.4. Applying sub-snow topography estimates

For the winter scene (Feb-2017 DEM), manual tracking by mapping exposed rock debris (Eq. (4)), and an optimization of the scale factor based on the snow depths was applied (Eq. (7)). The manually mapped displacements were based on both aerial imagery and hillshade models from the UAV surveys. We were able to map the displacements of five exposed rocks. For the spring scene (Jun-2017 DEM), the optimization of the scale factor was based on snow-free elevations and snow-depth observations in active terrain (Eq. (5)). The snow-free areas in the Jun-2017 were mapped from an orthomosaic derived from the UAV imagery. The snow depths for both scenes were based on snow probing in combination with a GNSS (positional accuracy ≤ 2 cm at 1σ) survey of

observed depth locations (Fig. 1). There were 63 field-surveyed snow depth observations made over the rock glacier on February 22, 2017 and 58 on June 2, 2017.

Since the snow-free DEMs used in this study were obtained before (Z_{t_2}; Aug-2012) and after (Z_{t_1}; Oct-2017) the snow-covered DEMs (S_{t_0}; Jun and Feb-2017) the optimized scale factors $\hat{c}$ were determined by applying the transformation (Eqs. (5) and (7)) with a range of c values from 0.0 to 1.0 (with a step of 0.01). As c approaches 0 and 1 the resulting estimated DEM $\hat{Z}_{t_0}$ becomes closer to the snow-free DEMs Z_{t_1} (Oct-2017 DEM) and Z_{t_2} (Aug-2012 DEM), respectively. In this case, the scale values can be interpreted as an approximation of the proportion of surface movement occurring between the dates used for mapping surface deformation, where one step of 0.01 would be expected to represent 2.68 weeks until October 5, 2017 (or 4.4 cm of average creep movement of the rock glacier). This scale ratio was used to explore the general plausibility of the scale values by determining how far off they are from the actual time between the snow-covered DEM and the Oct-2017 DEM. An overview of the processes involved to estimate the sub-snow topography are presented in Fig. 2.

2.5. Error analysis

The performance of the sub-snow topography estimates was assessed by comparing the estimated snow depths to in-situ snow-probed measurements (Table 1). For each date, the snow depth errors were calculated for the estimated snow depths based on the untransformed snow-free DEMs (Oct-2017 and Aug-2012 DEMs) and the transformed snow-free DEMs (i.e., est. Jun-2017 or est. Feb-2017 DEMs). Since the Jun-2017 DEM contained snow-free areas, the performance of the estimated elevation model (est. Jun-2017 DEM) was also assessed using a GNSS field survey (positional accuracy ≤ 2 cm at 1σ) conducted on June 2, 2017. This survey allowed for validation of the est. Jun-2017 DEMs independent from the procedure used for optimizing the scale factor. For general comparison, the accuracy was calculated for stable and active terrain. In total 70 points located in exposed stable ($N = 35$) and active ($N = 35$) terrain were collected. These observed elevations were compared to the nearest grid cells in the Jun-2017 DEM and the est. Jun-2017 DEMs to measure the corresponding elevation errors. Additionally, the error relative to these GNSS surveyed locations to the Oct-2017 and the Aug-2017 DEM were measured as a benchmark for accuracy. The elevation and snow depth errors were reported using the interquartile range (IQR) and median relative absolute error (RAE) to account for the potential presence of outliers. The RMSE was also reported along with the IQR since it is a standard measure of accuracy for measuring elevation height and snow depths.

3. Results

3.1. Mapped surface deformations

The direction of the modelled surface displacements follows the general downslope path of the rock glacier, where the front is moving slightly northeast (Fig. 3). The stable areas were modelled as the areas adjacent to and along the sides of the rock glacier. The faster movements (> 1.0 m/yr) in the upper part of the rock glacier occurred in an area where the hillslope is relatively steep compared to the rest of the rock glacier body. There were also modelled fast movements (> 1.4 m/yr) on the steep rock face (Fig. 3B). These high displacement magnitudes on the rock face were not expected since this is a stable outcrop and indicate an area where the image alignment was difficult.

3.2. Optimal scale factors

The scale factors optimized using the snow-free elevation and snow-depth data were in general agreement (Fig. 4). The snow-free areas ($\hat{c} = 0.08$) and snow-depth ($\hat{c} = 0.08$) optimized scale factors for the est. Jun-2017 DEM were the same. The mapping based ($\hat{c} = 0.14$) and snow-depth optimized ($\hat{c} = 0.13$) scale factors for the est. Feb-2017 DEM differed by a single step (0.01 or 4.4 cm of average creep movement of the rock glacier). The scale factors were also plausible in terms of their expected displacement on the respective dates (Fig. 5). The expected scale factors based on the number of weeks that the June 2, 2017 (18) and February 22, 2017 (32) dates were before October 5, 2017 were 0.07 and 0.12, respectively. Optimized scale factors for June and February were found within 3 weeks of these expected values (Fig. 5).

3.3. Performance of estimated DEMs

As assessed using GNSS field observations in snow-free areas, the est. Jun-2017 DEM had the best overall vertical accuracy compared to the Oct-2017 and Aug-2012 DEMs (Table 2). The spread of the vertical errors in the est. Jun-2017 DEM (IQR = 5.5 cm) was also considerably lower for the active terrain compared to the Oct-2017 (21.8 cm) and Aug-2012 (54.4 cm) DEMs (Fig. 6, Table 2). The est. Jun-2017 DEM also had a lower spread in errors for active terrain compared to the Jun-2017 DEM. The spread of the errors in the stable terrain were generally similar between the snow-free DEMs with a range in IQRs from 8.4 cm to 9.0 cm (Table 2). Additionally, there was a tendency to overestimate the elevations in stable terrain and underestimate them in active terrain.

The comparison to the GNSS field observations also illustrated that the reliability of the snow-free DEMs decreases as the time between acquisitions dates increases. The Oct-2017 and Aug-2012 DEMs tended to underestimate the actual elevations in snow free areas (Fig. 6). The Aug-2012 had the highest overall error (RMSE = 51.3 cm, IQR = 50.9 cm).

The differences in elevations of the DEMs relative to the snow-free areas in the June-2017 DEM were used to determine which elevation model best represented the sub-snow topography on June 2, 2017. Overall, the est. Jun-2017 DEM had the highest similarity to the snow-free cell locations in the June-2017 DEM followed by the Oct-2017 DEM (Table 3). The higher similarity of the est. Jun-2017 DEM compared with the Oct-2017 DEM was mainly attributed to the better performance of the est. Jun-2017 DEM to represent the sub-snow topography in active terrain (Table 3).

The highest differences to the Jun-2017 DEM were observed in areas where mass-wasting processes additional to the overall rock glacier creep occur (Fig. 7). Elevations in the est. Jun-2017 DEM and the Oct-2017 DEM were underestimated where small debris channels formed on the rock glacier front. They were also underestimated in an area just next to the steep rock face, located in the southeast corner of the scene, where there is evidence of a debris flow. The elevations on the rock glacier front for the est. Jun-2017 and Oct-2017 DEM were for the majority overestimated. However, the front in the est. Jun-2017 DEM appears to have a smaller area of overestimation. The Aug-2012 DEM suffered from high elevation underestimation at the front slope, and high overestimation in snow-free areas located in areas upslope of the rock glacier front.

In terms of reducing snow depths errors for the June data, the estimated DEMs had the lowest errors measured by the IQR and median RAE compared to the untransformed DEMs (Table 3). As previously observed in the snow-free locations (Table 2), the better performance of the estimated DEMs was related to reducing errors in active terrain. Except for the Aug-2012 DEM, the errors in snow-depth were similar in stable areas (Table 3). It was also observed that the June snow depths were generally underestimated in active terrain (all median values < -6.0 cm; Fig. 8A). The snow depth errors were considerably lower in stable terrain than in active terrain (IQR difference of up to 10 cm); however, the snow depth errors in the stable terrain also contained major outliers (Fig. 8A).

For the February data, the lower IQRs and median RAEs

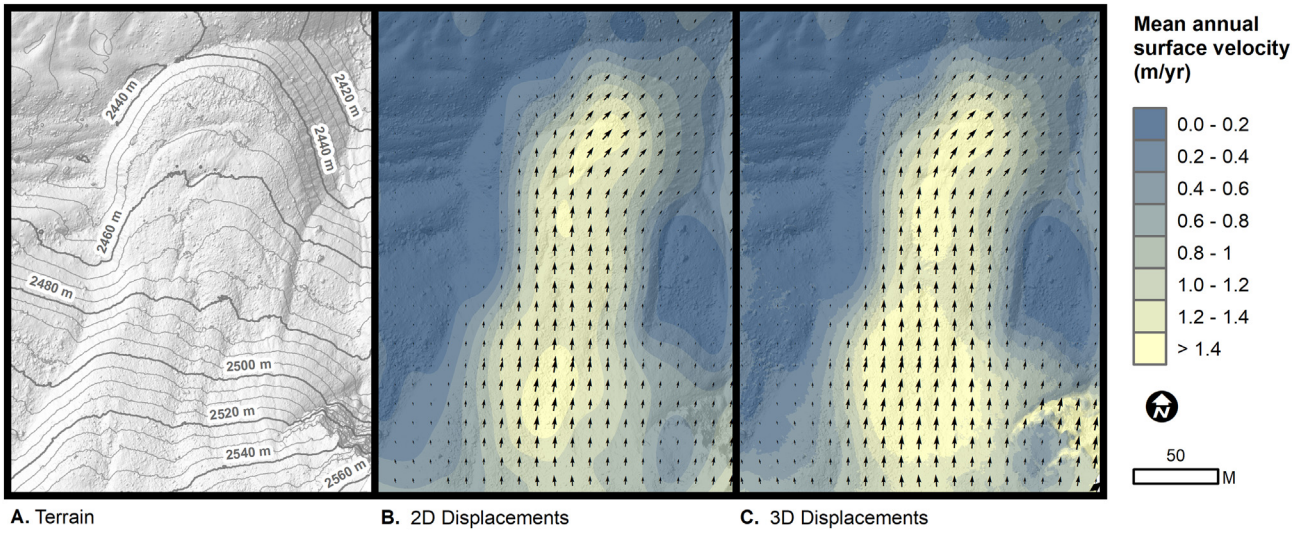

Fig. 3. A map of the study site terrain illustrated using a hillshade map and a 5 m contour interval (A.), and the 2D (B.) and 3D (C.) displacement fields obtained from a free-form deformation model based on B-splines. The displacements magnitudes are shown here as the mean annual surface velocities (m/yr) from 2012 to 2017. The size of the arrows depicting the direction of the rock glacier movement is proportional to the magnitude of the displacements.

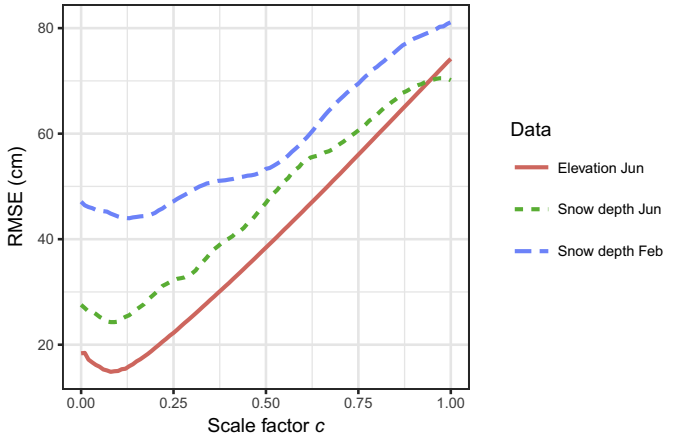

Fig. 4. The performance of scaled values for est. Jun- and Feb-2017 DEMs based on optimization using snow-free elevation grid cells (Jun-2017) and in-situ snow-depth measurements (Jun-2017 and Feb-2017).

demonstrate that the estimated elevation models performed better at estimating snow depths compared to the untransformed DEMs (Table 4). Like the June results, the spread of the snow depth errors was larger in active terrain (all IQRs > 22.7 cm) than in stable terrain (all IQRs < 9.6 cm).

By qualitatively examining the snow depth maps, it appears at the scale of meters that the general patterns were similar between the est. DEMs and the Oct-2017 DEM derived snow depths (Figs. 9A, B and 10A,

Table 2
Error in elevations relative to the snow-free GNSS measurements in the Jun-2017 DEM. The errors have been grouped into active (i.e., on the rock glacier) and stable terrain. The est. Jun-2017 DEM where $\hat{c} = 0.07$ was obtained from the expected scale factor on 2-Jun-2017 DEMs, and $\hat{c} = 0.08$ was obtained from optimization of the elevation and in-situ snow-depth measurements. The Oct-2017 and Aug-2017 were untransformed DEMs. The median and mean error are reported as measures of bias.

DEM	2-Jun-2017 GNSS elevation error (cm)			
	IQR	Median	RMSE	Mean
Overall				
Jun-2017	13.8	0.2	9.5	1.6
Est. Jun-2017 ($\hat{c} = 0.07$)	9.7	−2.8	13.4	−3.1
Est. Jun-2017 ($\hat{c} = 0.08$)	9.2	−1.9	13.5	−3.0
Oct-2017	17.2	−2.8	19.8	−7.8
Aug-2012	51.3	−6.8	50.9	−24.3
Active				
Jun-2017	8.1	−3.9	6.7	−4.1
Est. Jun-2017 ($\hat{c} = 0.07$)	5.0	−5.0	17.1	−8.6
Est. Jun-2017 ($\hat{c} = 0.08$)	5.5	−5.1	17.3	−8.3
Oct-2017	21.8	−12.0	26.8	−18.3
Aug-2012	54.4	−48.1	70.9	−49.6
Stable				
Jun-2017	7.3	8.0	11.7	7.4
Est. Jun-2017 ($\hat{c} = 0.07$)	8.9	2.8	8.2	2.4
Est. Jun-2017 ($\hat{c} = 0.08$)	9.0	2.9	8.2	2.4
Oct-2017	8.5	2.6	7.8	2.6
Aug-2012	8.4	1.5	12.8	1.1

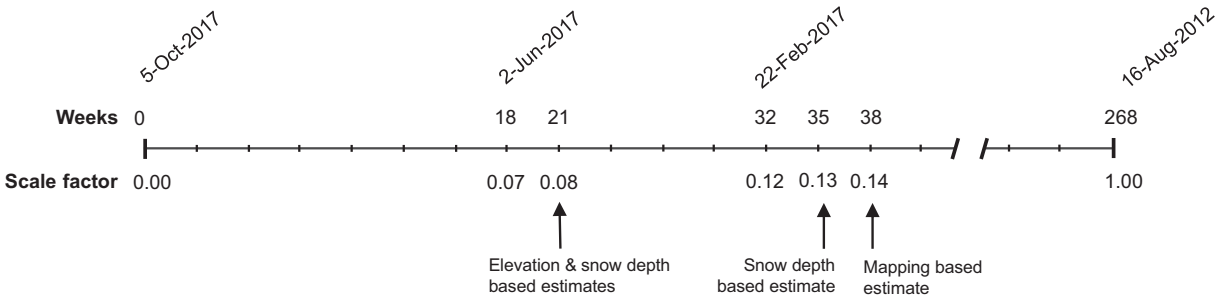

Fig. 5. Estimated scale factor c compared to expected weeks.

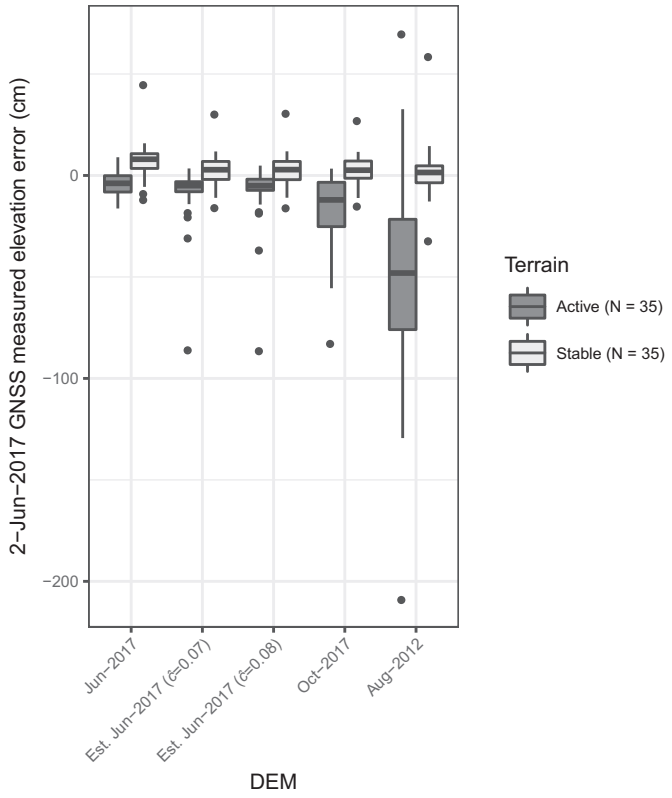

Fig. 6. Elevation errors of the Jun-2017 DEMs based on GNSS surveyed elevations of snow-free areas. The errors have been grouped into active (i.e., on the rock glacier) and stable terrain. The est. Jun-2017 DEMs where $\hat{c} = 0.07$ were obtained from the expected scale factor on 2-Jun-2017, and $\hat{c} = 0.08$ was obtained from optimization of the elevation and in-situ snow-depth measurements. The Oct-2017 and Aug-2017 were untransformed DEMs.

B). However, by looking at the sub-meter scale (Figs. 9C and 10C), the pattern of snow depth varied substantially in the area on the rock glacier, particularly at the rock glacier front, and where compression ridges are present.

4. Discussion

4.1. Performance of the deformation model

The ability to improve the estimate of the sub-snow topography and to reduce errors in the resulting snow depths weighed heavily on the ability of the surface deformation model to correctly represent the spatial pattern of the rock glacier movement. Our model-based on non-rigid image registration using B-splines to model surface deformations appeared to perform well throughout most of the scene. The model displacement magnitudes and directions of the rock glacier movement and stable areas agreed with our knowledge of the scene. The GNSS-assessed accuracy of the est. Jun-2017 DEMs were most similar to the snow-free areas of the Jun-2017 snow-covered DEM, and the elevation accuracy was nearly 50% better than the Oct-2017 DEM. Additionally, the overall pattern of the displacements on the rock glacier matched well to the patterns obtained using the IMCORR image matching algorithm in a study by Bodin et al. (2018). However, there were some areas where it was clear where the deformation model did not perform well (Fig. 3).

The rock glacier front was one of the most difficult areas for the registration algorithm to perform. The movement of rock debris on the rock glacier front was more dynamic than the rest of the rock glacier body due to the steep slope. Here, the main mass-wasting processes were rock-falls and small debris slides. This dynamic nature of the rock glacier front, or any area on the rock glacier where more rapid mass wasting processes occur, can make it more difficult determine pixel correspondences. Alternatively, if features are identified on the rock glacier front, such as large boulders, we have to be cautious to map these correspondences, as it may result in modelling displacements that are unrelated to the overall rock glacier creep movement. It is likely that the errors in the deformation model related to other mass-wasting processes can be reduced by performing non-rigid registration using DEMs acquired in the snow-free period directly before and after the snow-cover season. However, deformations related to seasonal erosion (Bernard et al., 2017) and frost-heaving (Nolan et al., 2015) would still be difficult to spatially model since they occur locally beneath the snow-cover.

The steep rock face of a stable outcrop was also an area where the deformation model did not perform well. It is likely that the errors in vertical displacement for the steep rock face were due to vertical disagreements between the LiDAR Aug-2012 and SFM-MVS Oct-2017

Table 3
Differences in elevations relative to the snow-free areas in the Jun-2017 DEM, and the errors in snow-depth estimation for 2-Jun-2017 based on the comparison of snow-probed measurements and DEM-derived snow depths. The errors have been grouped into active (i.e., on the rock glacier) and stable terrain. The est. Jun-2017 DEMs where $\hat{c} = 0.07$ was obtained from the expected scale factor on 2-Jun-2017, and $\hat{c} = 0.08$ was obtained from optimization of the elevation and in-situ snow-depth measurements. The Oct-2017 and Aug-2017 were untransformed DEMs. The median and mean error are reported as measures of bias.

2-Jun-2017	Snow-free elevation difference (cm)				Snow depth error (cm)				Median RAE %	Median depth (cm)
DEM	IQR	Median	RMSE	Mean	IQR	Median	RMSE	Mean		
Overall										
Est. Jun-2017 ($\hat{c} = 0.07$)	9.5	−1.2	14.5	−2.3	12.2	−1.4	47.1	7.0	6.7	115.8
Est. Jun-2017 ($\hat{c} = 0.08$)	9.6	−1.3	14.6	−2.5	13.0	−1.4	47.0	6.8	6.6	114.9
Oct-2017	12.5	−1.8	16.1	−0.8	16.5	−0.9	47.8	8.1	7.4	118.4
Aug-2012	52.5	−6.4	61.0	−23.0	36.5	0.5	66.7	3.2	15.9	114.5
Active										
Est. Jun-2017 ($\hat{c} = 0.07$)	8.6	1.3	15.1	−0.5	15.5	−6.9	24.4	−5.2	8.9	94.8
Est. Jun-2017 ($\hat{c} = 0.08$)	8.6	1.3	14.9	−0.8	16.5	−7.1	24.3	−5.5	9.2	95.3
Oct-2017	15.8	2.1	18.4	1.6	19.5	−6.0	27.6	−3.2	11.0	93.0
Aug-2012	100.4	−18.4	75.1	−34.1	61.4	−21.6	70.5	−18.8	35.8	99.0
Stable										
Est. Jun-2017 ($\hat{c} = 0.07$)	5.1	−5.0	13.3	−5.7	9.9	1.4	61.1	18.3	5.3	166.3
Est. Jun-2017 ($\hat{c} = 0.08$)	5.2	−5.0	13.9	−5.7	9.7	1.4	61.1	18.3	5.0	166.3
Oct-2017	5.3	−4.9	10.7	−5.3	9.8	2.0	61.0	18.7	5.0	166.5
Aug-2012	12.1	−3.4	12.8	−2.4	17.0	4.9	62.9	23.7	5.1	172.2

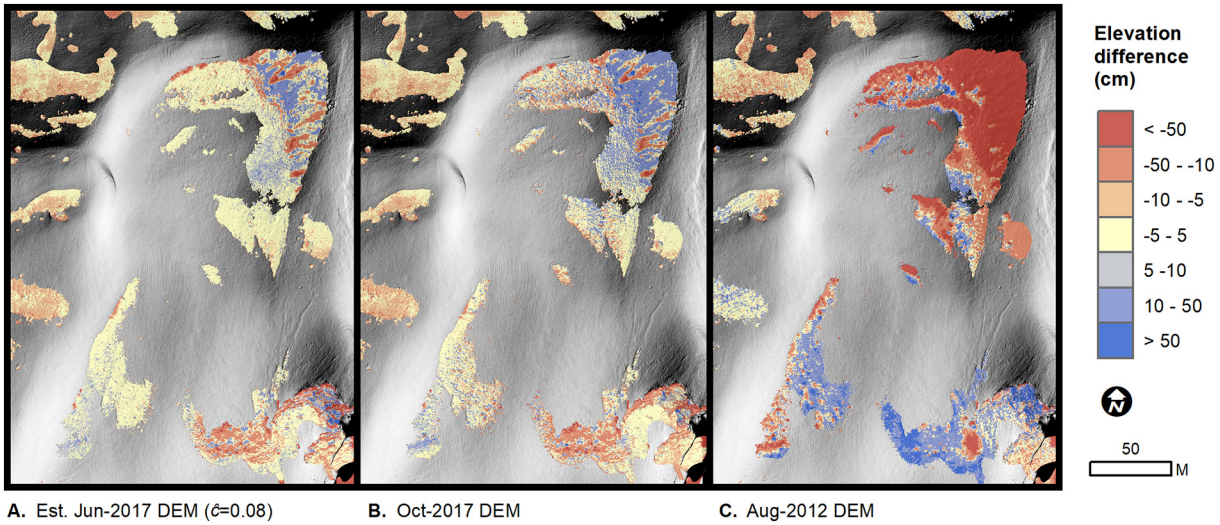

Fig. 7. Maps of the difference in elevations for the est. Jun-2017 ($\hat{c}$ = 0.08), Oct-2017 and Aug-2012 DEMs from the snow-free areas in the Jun-2017 DEM.

derived DEMs in this stable area. The vertical accuracy of DEMs derived from both airborne LiDAR and SFM-MVS data are known to deteriorate on steeper terrain (Hodgson and Bresnahan, 2004; Tonkin et al., 2014). To overcome this issue, it may be necessary to align the stable areas of these DEMs before performing registration on the entire scene. In general, more accurate SFM-MVS DEMs can be obtained by using lower UAV flying heights (Smith and Vericat, 2015; Goetz et al., 2018). Broad systematic errors in SFM-MVS DEMs can be mitigated using well-distributed high-quality GNSS measured ground control (Tonkin and Midgley, 2016; James et al., 2017a; James and Robson, 2014), and by including images taken at oblique angles to the ground surface in the UAV imagery collection (James and Robson, 2014).

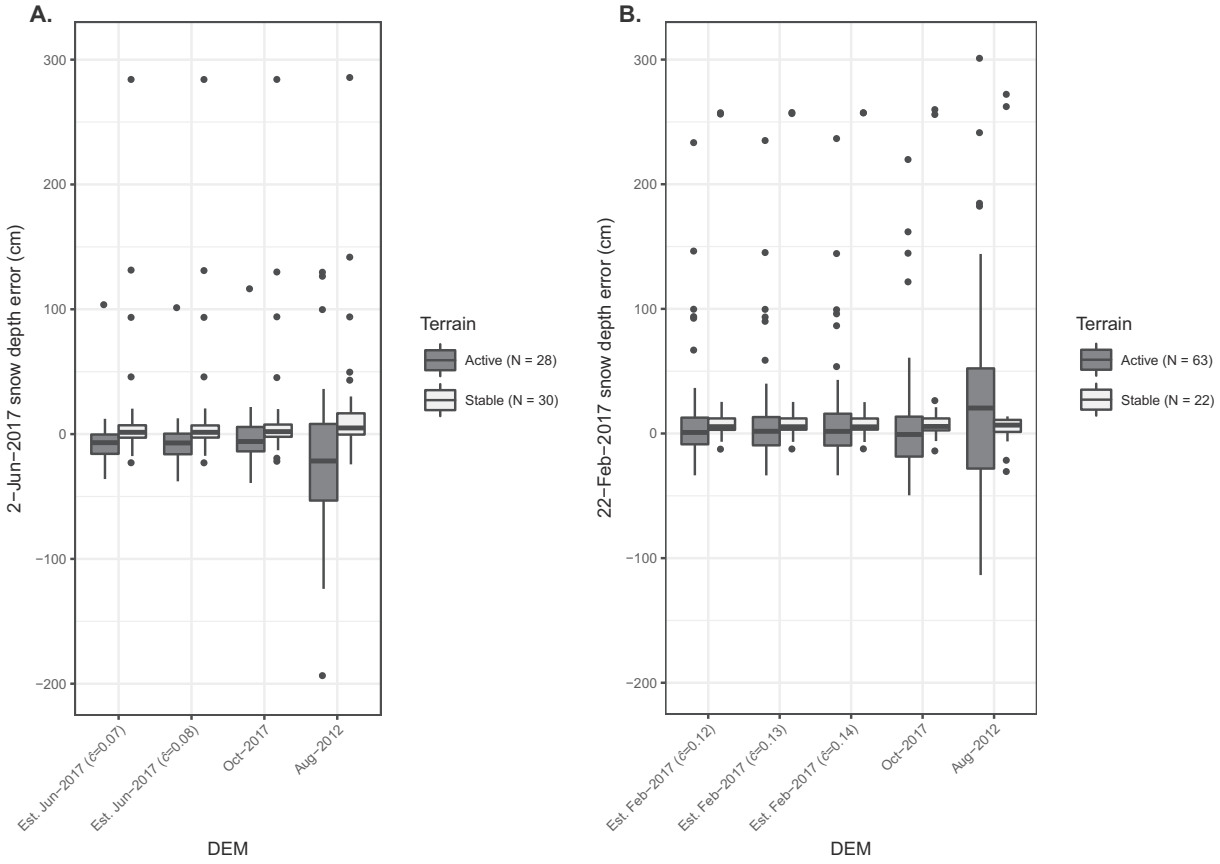

Fig. 8. Box plots of the error between snow-probed measured and the DEM-derived snow depths for 2-Jun-2017 (A.) and 22-Feb-2017 (B). The snow depth error has been grouped by active (i.e., on the rock glacier) and stable terrain. Est. Jun-2017 DEMs where $\hat{c}$ = 0.07 was obtained from the expected scale factor on 2-Jun-2017, and $\hat{c}$ = 0.08 was obtained from optimization of the elevation and in-situ snow-depth measurements. The est. Feb 2017 DEMs where $\hat{c}$ = 0.12 obtained from the expected scale factor on 22-Feb-2017, $\hat{c}$ = 0.13 from the optimization of the in-situ snow depth measurements, and $\hat{c}$ = 0.14 from the manually mapped displacements. The Oct-2017 and Aug-2017 were untransformed DEMs.

Table 4
Errors in snow-depth estimation for 22-Feb-2017 based on the comparison of snow-probed measurements and DEM-derived snow depths. The errors have been grouped into active (i.e., on the rock glacier) and stable terrain. The est. Feb 2017 DEMs where $\hat{c} = 0.12$ obtained from the expected scale factor on 22-Feb-2017, $\hat{c} = 0.13$ from the optimization of the in-situ snow depth measurements, and $\hat{c} = 0.14$ from the manually mapped displacements. The Oct-2017 and Aug-2017 were untransformed DEMs. The median and mean error are reported as measures of bias.

22-Feb-2017	Snow depth error (cm)				Median RAE %	Median depth (cm)
DEM	IQR	Median	RMSE	Mean		
Overall						
Est. Feb-2017 ($\hat{c} = 0.12$)	17.5	3.3	55.0	15.5	7.1	152.5
Est. Feb-2017 ($\hat{c} = 0.13$)	17.6	3.2	55.0	15.7	7.5	152.4
Est. Feb-2017 ($\hat{c} = 0.14$)	18.3	3.3	55.1	15.8	7.2	151.8
Oct-2017	23.1	3.7	57.0	14.2	10.1	152.0
Aug-2012	58.7	8.1	80.7	23.3	26.7	144.0
Active						
Est. Feb-2017 ($\hat{c} = 0.12$)	21.4	0.8	44.0	10.8	9.1	149.7
Est. Feb-2017 ($\hat{c} = 0.13$)	22.7	1.8	44.0	11.0	8.2	149.4
Est. Feb-2017 ($\hat{c} = 0.14$)	25.5	1.7	44.1	11.2	8.2	148.2
Oct-2017	32.0	−0.8	47.1	9.0	13.1	146.6
Aug-2012	80.4	20.4	80.5	22.1	35.8	141.0
Stable						
Est. Feb-2017 ($\hat{c} = 0.12$)	9.2	5.5	78.3	29.1	5.4	159.6
Est. Feb-2017 ($\hat{c} = 0.13$)	9.1	5.4	78.4	29.1	5.4	159.6
Est. Feb-2017 ($\hat{c} = 0.14$)	8.9	5.4	78.5	29.1	5.4	159.6
Oct-2017	9.6	5.6	78.7	29.0	4.9	159.1
Aug-2012	9.6	6.7	81.5	26.6	5.3	160.3

4.2. Finding the optimal the scale factor

The proposed methods for finding the optimal scale factor (i.e., manually mapping displacements, using probed snow depths, or using snow-free areas) were shown to produce estimates of the sub-snow topography that were more accurate than using the acquired snow-free DEM. During spring melt conditions containing snow-free areas, finding an optimal c was rather straightforward, and required no additional data collection. In contrast, finding the scale factor during the times of complete snow cover may require additional data.

Some winter scenes may have exposed debris that can be utilized to determine c, as demonstrated in this study. Yet, there will be occasions when the scene is completely snow covered. In this case, we illustrated how snow probed depths can be used to find an optimal c. If the DEMs are derived from UAV or terrestrial imagery (i.e., SFM-MVS 3D reconstruction), the required depths for optimization can be measured after image acquisition during the collection of ground control points. DEMs derived from SFM-MVS methods generally require the use of a network of GNSS surveyed ground control for accurate DEM construction (Tonkin and Midgley, 2016; James et al., 2017b). However, collecting snow probed depths can be challenging and dangerous depending on the given snow conditions and terrain complexity.

Although it was not initially proposed, we found that the expected scale factor determined as the proportional time before October 5, 2017 also produced estimated DEMs that reduced errors in the DEM representing the sub-snow surface and reduced the corresponding snow depth errors compared the Oct-2017 DEM. That is, given the rate of permafrost creep movement is rather constant, a suitable scaling factor can also be determined based on the date of the snow-covered scenes alone (as illustrated in Fig. 4) for occasions when the scene is completely snow covered.

The general agreement of the snow-free based and snow-depth based optimization of the scale factors illustrates a promising potential of manual snow depth probing, in combination with an accurate surface deformation model, to monitor interannual variations of permafrost creep during snow-covered periods. Since the scale factor can be

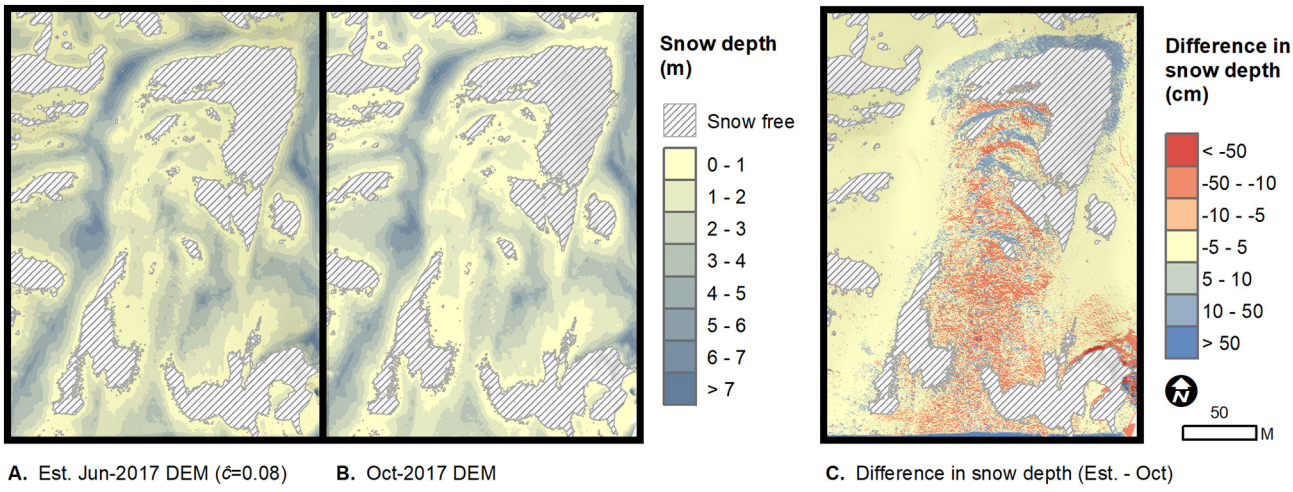

Fig. 9. Snow depth maps derived from the est. Jun-2017 DEM ($\hat{c} = 0.08$) (A.) and the Oct-2017 DEM (B.) for 2-Jun-2017, as well as a map of the difference in snow depth estimated by these DEMs (C.). Positive values in the difference map indicate areas where the est. Jun-2017 DEM derived snow depths were deeper than the Oct-2017 DEM derived snow depths.

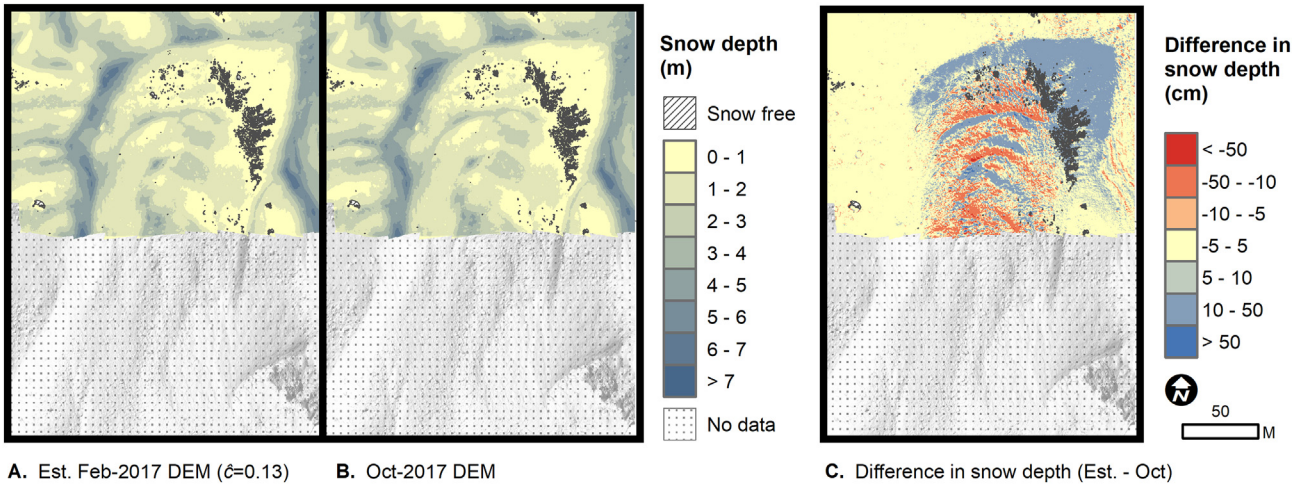

Fig. 10. Snow depth maps derived from the est. Feb-2017 DEM ($\hat{c} = 0.13$) (A.) and the Oct-2017 DEM (B.) for 22-Feb-2017, as well as a map of the difference in snow depth estimated by these DEMs (C.). Positive values in the difference map indicate areas where the est. Feb-2017 DEM derived snow depths were deeper than the Oct-2017 DEM derived snow depths.

expressed as the displacement rate relative to the time of one of the snow-free DEMs, seasonal variation may be observed by comparing the determined scale factors from snow probe surveys taken from a range of dates during the snow-covered period.

4.3. Snow depth errors

The reduction in snow depth errors related to using the estimated sub-snow surface DEM compared to the available snow-free DEM illustrates that surface deformation processes, such as permafrost creep, can lead to errors in high-resolution snow depths determined from differencing of DEMs. It also illustrates that kinematic models of the surface deformation can be used account for the permafrost creep related changes in topography between snow-covered and snow-free DEM acquisition dates to reduce errors in snow depth estimation.

In previous studies, the observed accuracies of snow depth estimated from high-resolution DEMs measured as the RMSE varied from of 7 cm to 30 cm (Nolan et al., 2015; Vander Jagt et al., 2015; Bühler et al., 2016; Harder et al., 2016; Michele et al., 2016). The overall accuracy of the est. Feb-2017 DEM snow depths (55 cm) and the est. Jun-2017 DEM snow depths were just outside of the range (47 cm). Outliers influenced these comparatively high RMSE values, ranging from 50 cm to 300 cm (Fig. 8), of the snow depth errors based on snow probe measurements. Since the majority of these outliers were overestimating the snow depths, we believe they may have been caused by occasions where the snow probe failed to penetrate the ground. To account for outliers in the survey data, the IQR was used as an alternative to the RMSE as a measure of the spread of the error.

Although the spread of error between the stable and active terrain in snow-free areas of the Jun-2017 DEMs were similar (min. IQR difference of 3.5 cm), the snow depth errors were lower on stable terrain than active terrain (6.8 cm). This dissimilarity in snow depth errors was also found with the Feb-2017 derived snow depths (13.6 cm). Given the surface of the stable terrain is not as rough as the active terrain, we believe this dissimilarity in snow depth errors may be due the challenges of obtaining accurate snow probe measurements in rock-debris filled terrain. That is, due to the higher variability in the surface topography, the accuracy of the snow probe measurements is more sensitive to GNSS-related location errors, and errors in reading of the snow depth caused by the snow probe penetration not being perpendicular to the ground. An improved GNSS surveyed snow depth sampling scheme could be applied in future works. For example, Harder et al. (2016) used the average snow depth measurement around a given location (i.e., within a 40 cm × 40 cm square) to account for snow depth reading errors related to the terrain's surface roughness when validating snow depths derived from high-resolution DEMs.

5. Conclusion

Errors in high-resolution snow depths derived from DEMs in mountain areas can be reduced by accounting for slope deformation, in this study by permafrost creep. This error reduction comes from being able to accurately model terrain surface deformations related to permafrost creep using non-rigid image registration. Multiple methods, which account for variable surface displacements over time, can be used to find a scaling factor to transform the displacement field for estimating a DEM representing the terrain surface beneath snow cover. In this study, they all resulted in estimated DEMs that provided an improved representation of the sub-snow topography relative to the original snow-free DEM. Surprisingly, a scale factor simply estimated based on the time before the snow-free scene resulted in an improvement of the estimate sub-snow topography similar to the optimization techniques.

Although the free-form deformation model based on B-splines for non-rigid image registration was performed for modelling only the movement of permafrost creep, we expect it could also be used to improve surface deformation modelling of other Earth surface processes such as landslide creep or glacial flow. Additionally, non-rigid image registration is not limited to DEM data, and can also be applied to optical remote sensing imagery to obtain displacement fields of the horizontal movement of Earth surface processes.

Acknowledgements

We would like to thank the Parc national des Ecrins and the Joseph Fourier Alpine Research Station (SAFJ) for their support, and everyone else who assisted us in the collection of this data. Also, thanks to the constructive comments provided by the anonymous referees. The Natural Sciences and Engineering Research Council of Canada (NSERC) through an Alexander Graham Bell Graduate Scholarship awarded to J. Goetz and funding from the Carl Zeiss Foundation awarded to A. Brenning have supported this research.

References

Abdalati, W., Krabill, W., 1999. Calculation of ice velocities in the Jakobshavn Isbrae area using airborne laser altimetry. Remote Sens. Environ. 67, 194–204.
Arenson, L.U., Kääb, A., O'Sullivan, A., 2016. Detection and analysis of ground

deformation in permafrost environments. Permafr. Periglac. Process. 27, 339–351.
Arganda-Carreras, I., Sorzano, C., Marabini, R., Carazo, J.-M., Ortiz-de Solorzano, C., Kybic, J., 2006. Consistent and elastic registration of histological sections using vector-spline regularization. Lecture notes in computer science. In: CVAMIA: Computer Vision Approaches to Medical Image Analysis, 4241/2006, pp. 85–95.
Avanzi, F., Bianchi, A., Cina, A., Michele, C. de, Maschio, P., Pagliari, D., Passoni, D., Pinto, L., Piras, M., Rossi, L., 2018. Centimetric accuracy in snow depth using unmanned aerial system photogrammetry and a MultiStation. Remote Sens. 10, 765.
Bernard, É., Friedt, J.M., Tolle, F., Griselin, M., Marlin, C., Prokop, A., 2017. Investigating snowpack volumes and icing dynamics in the moraine of an Arctic catchment using UAV photogrammetry. Photogramm. Rec. 32, 497–512.
Bhardwaj, A., Sam, L., Bhardwaj, A., Martín-Torres, F.J., 2016. LiDAR remote sensing of the cryosphere. Present applications and future prospects. Remote Sens. Environ. 177, 125–143.
Blöschl, G., 1999. Scaling issues in snow hydrology. Hydrol. Process. 13, 2149–2175.
Bodin, X., Thibert, E., Fabre, D., Ribolini, A., Schoeneich, P., Francou, B., Reynaud, L., Fort, M., 2009. Two decades of responses (1986 - 2006) to climate by the Laurichard rock glacier, French Alps. Permafr. Periglac. Process. 20, 331–344.
Bodin, X., Thibert, E., Sanchez, O., Rabatel, A., Jaillet, S., 2018. Multi-annual kinematics of an active rock glacier quantified from very high-resolution DEMs. An application-case in the French Alps. Remote Sens. 10, 547.
Bühler, Y., Marty, M., Ginzler, C., 2012. High resolution DEM generation in high-alpine terrain using airborne remote sensing techniques. Trans. GIS 16, 635–647.
Bühler, Y., Marty, M., Egli, L., Veitinger, J., Jonas, T., Thee, P., Ginzler, C., 2015. Snow depth mapping in high-alpine catchments using digital photogrammetry. Cryosphere 9, 229–243.
Bühler, Y., Adams, M.S., Bösch, R., Stoffel, A., 2016. Mapping snow depth in alpine terrain with unmanned aerial systems (UAS). Potential and limitations. Cryosphere 1075–1088.
Crum, W.R., Hartkens, T., Hill, D.L.G., 2004. Non-rigid image registration: theory and practice. Br. J. Radiol. 77, S140–S153.
Dall'Asta, E., Forlani, G., Roncella, R., Santise, M., Diotri, F., Di Morra Cella, U., 2017. Unmanned aerial systems and DSM matching for rock glacier monitoring. ISPRS J. Photogramm. Remote Sens. 127, 102–114.
Debella-Gilo, M., Kääb, A., 2011. Sub-pixel precision image matching for measuring surface displacements on mass movements using normalized cross-correlation. Remote Sens. Environ. 115, 130–142.
Debella-Gilo, M., Kääb, A., 2012. Measurement of surface displacement and deformation of mass movements using least squares matching of repeat high resolution satellite and aerial images. Remote Sens. 4, 43–67.
Deems, J.S., Fassnacht, S.R., Elder, K.J., 2006. Fractal distribution of snow depth from Lidar data. J. Hydrometeorol. 7, 285–297.
Deems, J.S., Painter, T.H., Finnegan, D.C., 2013. Lidar measurement of snow depth. A review. J. Glaciol. 59, 467–479.
Delaloye, R., Perruchoud, E., Avian, M., Kaufmann, V., Bodin, X., Hausmann, H., Ikeda, A., Kääb, A., Kellerer-Pirklbauer, A., Krainer, K., Lambiel, C., Mihajlovic, D., Staub, B., Roer, I., Thibert, E., 2008. Recent interannual variations of rock glacier creep in the European Alps. In: Kane, D.L., Hinkel, K.M. (Eds.), Proceedings of the 9th International Conference on Permafrost, pp. 343–348.
Draebing, D., Haberkorn, A., Krautblatter, M., Kenner, R., Phillips, M., 2017. Thermal and mechanical responses resulting from spatial and temporal snow cover variability in permafrost rock slopes, Steintaelli, Swiss Alps. Permafr. Periglac. Process. 28, 140–157.
Elder, K., Dozier, J., Michaelsen, J., 1991. Snow accumulation and distribution in an alpine watershed. Water Resour. Res. 27, 1541–1552.
Erickson, T.A., Williams, M.W., Winstral, A., 2005. Persistence of topographic controls on the spatial distribution of snow in rugged mountain terrain, Colorado, United States. Water Resour. Res. 41, 1–17.
Evans, A.N., 2000. Glacier surface motion computation from digital image sequences. IEEE Trans. Geosci. Remote Sens. 38, 1064–1072.
Ghuffar, S., Székely, B., Roncat, A., Pfeifer, N., 2013. Landslide displacement monitoring using 3D range flow on airborne and terrestrial LiDAR data. Remote Sens. 5, 2720–2745.
Goetz, J., Brenning, A., Marcer, M., Bodin, X., 2018. Modeling the precision of structure-from-motion multi-view stereo digital elevation models from repeated close-range aerial surveys. Remote Sens. Environ. 210, 208–216.
Grocott, T., Thomas, P., Münsterberg, A.E., 2016. Atlas toolkit: fast registration of 3D morphological datasets in the absence of landmarks. Sci. Rep. 6, 20732.
Grünewald, T., Stötter, J., Pomeroy, J.W., Dadic, R., Moreno Baños, I., Marturià, J., Spross, M., Hopkinson, C., Burlando, P., Lehning, M., 2013. Statistical modelling of the snow depth distribution in open alpine terrain. Hydrol. Earth Syst. Sci. 17, 3005–3021.
Grünewald, T., Bühler, Y., Lehning, M., 2014. Elevation dependency of mountain snow depth. Cryosphere 8, 2381–2394.
Haberkorn, A., Phillips, M., Kenner, R., Rhyner, H., Bavay, M., Galos, S.P., Hoelzle, M., 2016. Thermal regime of rock and its relation to snow cover in steep alpine rock walls. Gemsstock, central swiss alps. Geogr. Ann. Ser. A 97, 579–597.
Haeberli, W., Hallet, B., Arenson, L., Elconin, R., Humlum, O., Kääb, A., Kaufmann, V., Ladanyi, B., Matsuoka, N., Springman, S., Mühll, D.V., 2006. Permafrost creep and rock glacier dynamics. Permafr. Periglac. Process. 17, 189–214.
Harder, P., Schirmer, M., Pomeroy, J., Helgason, W., 2016. Accuracy of snow depth estimation in mountain and prairie environments by an unmanned aerial vehicle. Cryosphere 10, 2559–2571.
Hasler, A., Gruber, S., Haeberli, W., 2011. Temperature variability and offset in steep alpine rock and ice faces. Cryosphere 5, 977–988.
Heid, T., Kääb, A., 2012. Evaluation of existing image matching methods for deriving glacier surface displacements globally from optical satellite imagery. Remote Sens. Environ. 118, 339–355.
Helfricht, K., Schöber, J., Seiser, B., Fischer, A., Stötter, J., Kuhn, M., 2012. Snow accumulation of a high alpine catchment derived from LiDAR measurements. Adv. Geosci. 32, 31–39.
Hill, D.L.G., Batchelor, P.G., Holden, M., Hawkes, D.J., 2001. Medical image registration. Phys. Med. Biol. 46, R1–R45.
Hodgson, M.E., Bresnahan, P., 2004. Accuracy of airborne Lidar-derived elevation: empirical assessment and error budget. Photogrammetric engineering and remote. Photogramm. Eng. Remote. Sens. 331–339.
Ikeda, A., Matsuoka, N., Kääb, A., 2008. Fast deformation of perennially frozen debris in a warm rock glacier in the Swiss Alps. An effect of liquid water. J. Geophys. Res. 113, 212.
James, M.R., Robson, S., 2014. Mitigating systematic error in topographic models derived from UAV and ground-based image networks. Earth Surf. Process. Landf. 39, 1413–1420.
James, M.R., Robson, S., d'Oleire-Oltmanns, S., Niethammer, U., 2017a. Optimising UAV topographic surveys processed with structure-from-motion. Ground control quality, quantity and bundle adjustment. Geomorphology 280, 51–66.
James, M.R., Robson, S., d'Oleire-Oltmanns, S., Niethammer, U., 2017b. Optimising UAV topographic surveys processed with structure-from-motion. Ground control quality, quantity and bundle adjustment. Geomorphology 280, 51–66.
Johnson, H.J., Christensen, G.E., 2002. Consistent landmark and intensity-based image registration. IEEE Trans. Med. Imaging 21, 450–461.
Kääb, A., 2002. Monitoring high-mountain terrain deformation from repeated air- and spaceborne optical data. Examples using digital aerial imagery and ASTER data. ISPRS J. Photogramm. Remote Sens. 57, 39–52.
Kääb, A., 2005. Combination of SRTM3 and repeat ASTER data for deriving alpine glacier flow velocities in the Bhutan Himalaya. Remote Sens. Environ. 94, 463–474.
Kääb, A., Kaufmann, V., Ladstädter, R., Eiken, T., 2003. Rock glacier dynamics: Implications from high-resolution measurements of surface velocity fields. In: Phillips, M., Springman, S., Arenson, L.U. (Eds.), Permafrost: Proceedings of the Eighth International Conference on Permafrost. Balkema, pp. 501–506.
Kellerer-Pirklbauer, A., Delaloye, R., Lambiel, C., Gärtner-Roer, I., Kaufmann, V., Scapozza, C., Krainer, K., Staub, B., Thibert, E., Bodin, X., Fischer, A., Hartl, L., 2018. Interannual variability of rock glacier flow velocities in the European Alps. In: Deline, P., Bodin, X., Ravanel, L. (Eds.), 5th European Conference on Permafrost, Book of Abstracts, pp. 396–397.
Komsta, Ł., Cieśla, Ł., Bogucka-Kocka, A., Józefczyk, A., Kryszeń, J., Waksmundzka-Hajnos, M., 2011. The start-to-end chemometric image processing of 2D thin-layer videoscans. J. Chromatogr. A 1218, 2820–2825.
Kraaijenbrink, P., Meijer, S.W., Shea, J.M., Pellicciotti, F., Jong, S.M. de, Immerzeel, W.W., 2016. Seasonal surface velocities of a Himalayan glacier derived by automated correlation of unmanned aerial vehicle imagery. Ann. Glaciol. 57, 103–113.
Ku, T., Swaney, J., Park, J.-Y., Albanese, A., Murray, E., Cho, J.H., Park, Y.-G., Mangena, V., Chen, J., Chung, K., 2016. Multiplexed and scalable super-resolution imaging of three-dimensional protein localization in size-adjustable tissues. Nat. Biotechnol. 34, 973–981.
Lowe, D.G., 2004. Distinctive image features from scale-invariant keypoints. Int. J. Comput. Vis. 60, 91–110.
Luetschg, M., Haeberli, W., 2007. Permafrost evolution in the Swiss Alps in a changing climate and the role of the snow cover. Nor. Geol. Tidsskr. 59, 78–83.
Marti, R., Gascoin, S., Berthier, E., Pinel, M. de, Houet, T., Laffly, D., 2016. Mapping snow depth in open alpine terrain from stereo satellite imagery. Cryosphere 10, 1361–1380.
Matsuura, S., Asano, S., Okamoto, T., Takeuchi, Y., 2003. Characteristics of the displacement of a landslide with shallow sliding surface in a heavy snow district of Japan. Eng. Geol. 69, 15–35.
Michele, C. de, Avanzi, F., Passoni, D., Barzaghi, R., Pinto, L., Dosso, P., Ghezzi, A., Gianatti, R., Della Vedova, G., 2016. Using a fixed-wing UAS to map snow depth distribution. An evaluation at peak accumulation. Cryosphere 10, 511–522.
Nolan, M., Larsen, C., Sturm, M., 2015. Mapping snow depth from manned aircraft on landscape scales at centimeter resolution using structure-from-motion photogrammetry. Cryosphere 9, 1445–1463.
Okamoto, T., Matsuura, S., Larsen, J.O., Asano, S., Abe, K., 2018. The response of pore water pressure to snow accumulation on a low-permeability clay landslide. Eng. Geol. 242, 130–141.
Prokop, A., Schirmer, M., Rub, M., Lehning, M., Stocker, M., 2008. A comparison of measurement methods. Terrestrial laser scanning, tachymetry and snow probing for the determination of the spatial snow-depth distribution on slopes. Ann. Glaciol. 49, 210–216.
Rueckert, D., Sonoda, L.I., Hayes, C., Hill, D.L., Leach, M.O., Hawkes, D.J., 1999. Nonrigid registration using free-form deformations: application to breast MR images. IEEE Trans. Med. Imaging 18, 712–721.
Scambos, T.A., Dutkiewicz, M.J., Wilson, J.C., Bindschadler, R.A., 1992. Application of image cross-correlation to the measurement of glacier velocity using satellite image data. Remote Sens. Environ. 42, 177–186.
Schindelin, J., Rueden, C.T., Hiner, M.C., Eliceiri, K.W., 2015. The ImageJ ecosystem: an open platform for biomedical image analysis. Mol. Reprod. Dev. 82, 518–529.
Shepard, D., 1968. A two-dimensional interpolation function for irregularly-spaced data. In: Blue, R.B., Rosenberg, A.M. (Eds.), Proceedings of the 1968 23rd ACM National Conference, pp. 517–524.
Smith, M.W., Vericat, D., 2015. From experimental plots to experimental landscapes. Topography, erosion and deposition in sub-humid badlands from structure-from-motion photogrammetry. Earth Surf. Process. Landf. 40, 1656–1671.
Sturm, M., 2015. White water. Fifty years of snow research in WRR and the outlook for

the future. Water Resour. Res. 51, 4948–4965.
Swift, D.A., Cook, S., Heckmann, T., Moore, J., Gärther-Roer, I., Korup, O., 2014. Ice and snow as landforming agents. In: Haeberli, W., Whiteman, C. (Eds.), Snow and Ice-related Hazards, Risks and Disasters. Elsevier, pp. 167–199.
Thibert, E., Bonnefoy-Demongeot, M., Finance, F., Bodin, X., 2018. Extracting the time signal in surface velocity changes along 3 decades at Laurichard rock glacier (French Alps). In: Deline, P., Bodin, X., Ravanel, L. (Eds.), 5th European Conference on Permafrost, Book of Abstracts, pp. 615–616.
Tonkin, T., Midgley, N., 2016. Ground-control networks for image based surface reconstruction. An investigation of optimum survey designs using UAV derived imagery and structure-from-motion photogrammetry. Remote Sens. 8, 786.
Tonkin, T.N., Midgley, N.G., Graham, D.J., Labadz, J.C., 2014. The potential of small unmanned aircraft systems and structure-from-motion for topographic surveys. A test of emerging integrated approaches at Cwm Idwal, North Wales. Geomorphology 226, 35–43.
Vander Jagt, B., Lucieer, A., Wallace, L., Turner, D., Durand, M., 2015. Snow depth retrieval with UAS using photogrammetric techniques. Geosciences 5, 264–285.
Winstral, A., Marks, D., Gurney, R., 2013. Simulating wind-affected snow accumulations at catchment to basin scales. Adv. Water Resour. 55, 64–79.
Yoo, T.S., 2004. Insight Into Images. Principles and Practice for Segmentation, Registration, and Image Analysis. A K Peters/CRC Press, New York.